arXiv:1406.5677v3 [gr-qc] 21 Apr 2015

Using iron line reverberation and spectroscopy to distinguish Kerr and non-Kerr black holes

Jiachen Jiang,[a] **Cosimo Bambi,**[a,1] **and James F. Steiner** [b,2]

[a]Center for Field Theory and Particle Physics and Department of Physics,
Fudan University, 220 Handan Road, 200433 Shanghai, China
[b]Harvard-Smithsonian Center for Astrophysics,
60 Garden Street, Cambridge, MA 02138, United States

E-mail: jcjiang12@fudan.edu.cn, bambi@fudan.edu.cn, jsteiner@cfa.harvard.edu

Abstract. The iron Kα line commonly observed in the X-ray spectrum of both stellar-mass and supermassive black hole candidates is produced by the illumination of a cold accretion disk by a hot corona. In this framework, the activation of a new flaring region in the hot corona imprints a time variation on the iron line spectrum. Future X-ray facilities with high time resolution and large effective areas may be able to measure the so-called 2-dimensional transfer function; that is, the iron line profile detected by a distant observer as a function of time in response to an instantaneous flare from the X-ray primary source. This work is a preliminary study to determine if and how such a technique can provide more information about the spacetime geometry around the compact object than the already possible measurements of the time-integrated iron line profile. Within our simplified model, we find that a measurement of iron line reverberation can improve constraints appreciably given a sufficiently strong signal, though that most of the information is present in the time-integrated spectrum. Our aim is to test the Kerr metric. We find that current X-ray facilities and data are unable to provide strong tests of the Kerr nature of supermassive black hole candidates. We consider an optimistic case of 10^5 iron line photons from a next-generation data set. With such data, the reverberation model improves upon the spectral constraint by an order of magnitude.

Keywords: astrophysical black holes, modified gravity, X-rays

[1]Corresponding author
[2]Hubble Fellow

Contents

1 Introduction **1**

2 Iron line reverberation **4**
2.1 The corona-disk model in lamppost geometry 4
2.2 Line reverberation from an on-axis coronal flare 5
2.3 The 2D transfer function for a Kerr background 6

3 The 2D transfer function for non-Kerr backgrounds **9**

4 Comparison of Kerr and non-Kerr models **10**
4.1 Role of the model parameters 13
4.2 A non-Kerr black hole example 16

5 Discussion **19**

6 Summary and conclusions **20**

1 Introduction

In 4-dimensional general relativity, a black hole (BH) is a relatively simple object. Neglecting a possible non-vanishing electric charge, the spacetime geometry is described by the Kerr solution and the object is completely specified by the value of its mass M and of its spin parameter $a_* = a/M = J/M^2$, where J is the BH spin angular momentum [1–3]. If we know M and a_*, all the properties of the spacetime can be calculated from these two quantities. Astrophysical BH candidates are grouped into two classes: (1) supermassive compact bodies in active galactic nuclei (AGN), hosting masses $M \sim 10^5 - 10^{10}\ M_\odot$; and (2) compact objects in X-ray binary systems with masses $M \approx 5 - 20\ M_\odot$ [4]. Both object classes are widely accepted to be BHs; on this basis, the spacetime geometry around them should therefore be well described by the Kerr solution. Indeed, initial deviations from the Kerr metric could be quickly radiated away through the emission of gravitational waves [5, 6]. Any initial non-vanishing electric charge would be quickly neutralized because of the highly ionized host environment of these objects [7]. The deviation induced by the presence of an accretion disk is usually completely negligible, because the disk mass is many orders of magnitude smaller than the mass of the BH candidate [8].

However, current observations cannot unambiguously confirm the Kerr BH paradigm. For the time being, our principal insight is through robust measurements of the masses of these objects. Such measurements are obtained through dynamical studies which employ the orbital motion of nearby or companion stars. From these measurements, one can conclude that stellar-mass BH candidates in X-ray binary systems are too massive to be neutron or quark stars for any plausible matter equation of state [9–12], while supermassive BH candidates at the center of galaxies are surely too heavy, compact, and old to be clusters of neutron stars, since the expected cluster lifetime due to evaporation and physical collisions would be shorter than the age of these systems [13]. The non-observation of thermal radiation emitted by the possible surface of these objects is usually interpreted as evidence for the existence of

an event (or at least of an apparent) horizon [14, 15]. In the end, these considerations lead one to conclude that astrophysical BH candidates are most readily explained as Kerr BHs in the framework of conventional physics, and that in order for them to be something else would only be natural in presence of new physics.

Nevertheless, general relativity has been tested only for weak gravitational fields, while the theory is almost unexplored in the limit of strong gravity [16]. Theoretical arguments in support of the Kerr BH hypothesis are thus not completely satisfactory, and one would like to find observational tests of whether the spacetime geometry around these objects is really described by the Kerr metric, especially in light of recent novel considerations which suggest the possibility of macroscopic deviations from classical predictions [17–19]. The original idea of testing the Kerr nature of astrophysical BH candidates was put forward about 20 years ago in Ref. [20], where a test was proposed using the gravitational waves emitted by a system of a stellar-mass compact object orbiting around a supermassive BH candidate. This testing ground was further explored by other authors [21–23]. More recently, there have been significant efforts examining possible tests of the Kerr BH hypothesis from the properties of the electromagnetic radiation emitted by the accretion disks of these systems. Such tests have been proposed using both present X-ray data as well as future observations in the X-ray, NIR, sub-mm, and radio bands [24–41]. For a review on the subject, see e.g. [42, 43] and references therein.

Today, there are two techniques commonly employed in probing the spacetime geometry around astrophysical BH candidates; that is, the continuum-fitting method [44–47] and the analysis of the iron Kα line [48–51]. These two techniques have been developed to estimate the spin parameter of BH candidates under the assumption that the spacetime geometry around them is described by the Kerr metric. Both also rely on the assumption that the inner-edge of the accretion disk is located at the innermost stable circular orbit (ISCO)[1], an assertion which is grounded in the observed constancy of accretion-disk inner radii [52]. The extension to non-Kerr backgrounds to test the Kerr nature of BH candidates is straightforward [24–30]. Recently, there has been an increasing interest in methods exploiting the time domain, in particular in the relativistic precession model [55, 56] and eclipse mapping [57, 58]. Even these techniques can be potentially used to test the Kerr metric [59].

To test the nature of BH candidates we can use an approach similar to the Parametrized Post-Newtonian (PPN) formalism of Solar System experiments [16]. One assumes a general background metric with some free parameters to be determined by observations. In the case of general relativity, the exact value of these parameters is known and one wants to check if the measurements of these parameters is consistent with the values required by general relativity. Unfortunately, at present there is not a framework as general as the PPN formalism to test the Kerr BH hypothesis. One can anyway consider a BH spacetime in which the compact object is specified by a mass M, a spin parameter a_*, and at least one deformation parameter. The latter measures possible deviations from the Kerr solution, which is recovered when the deformation parameter vanishes. One can then try to constrain the deformation parameter and see if observations require a non-Kerr element or not.

In general, however, it is not easy to constrain the deformation parameter. Critically, the continuum-fitting and iron line measurements seem able to measure only one parameter of

[1] Here it is clearly important to select the sources in which the inner edge of the disk is at the ISCO radius. This is likely the case when the accretion luminosity is between a few percent and about 30% the Eddington luminosity, which is a selection criterion commonly employed in the continuum-fitting method [47, 52–54]. We note that when advection becomes important the inner edge of the disk deviates predictably from the ISCO.

the spacetime geometry close to BH candidates. In other words, there is a strong degeneracy between any constraint on spin and deformation parameters, and therefore a single measurement is only able to constrain a combination of these two quantities. By measuring different relativistic effects using a variety of techniques for the same source, one can potentially break such degeneracy [60–63]. The current data fall short of providing strong independent constraints, but it will be hopefully achievable in the future. With current observations, we can at most exclude some very exotic BH alternatives, like compact objects without event horizon [64] and some classes of wormholes [65]. In the case of objects that look like very-fast rotating Kerr BHs, it is generally possible to obtain a bounded constraint ellipse along the spin–deformation parameter plane [66]; usually it is difficult for deformations and low spin to mimic a Kerr BH with spin parameter close to 1 (but see Ref. [67]).

In this Paper, we aim to study the information provided by iron line reverberation to test the Kerr nature of BH candidates. The exact origin and geometry of the corona that produces the iron line is not known, although some progresses have been achieved [68], but the line exhibits a high degree of variability on short timescales which seems to be associated with the activation of new flaring regions. This, in turn, spawns temporal variations in the iron line, owing to the different propagation time for different photon paths. Because of the limited count rates in the iron line with current X-ray facilities, present observations are integrated over many thousands of seconds. This causes a loss of information. Future X-ray facilities with large effective areas may be able to study the temporal change in response to the activation of new flares[2]. Reverberation of the line can be exploited to gain insight into the system [70–72]. Here, we aim to figure out the advantage of the study of line reverberation to constrain possible deviations from the Kerr metric around BH candidates. The key-quantity to study is the 2-dimensional (2D) transfer function, which essentially corresponds to the time dependent iron line profile produced by an X-ray source emitting an instantaneous flare. While the advantage of reverberation observations over pure iron line spectroscopy depends on the quality of the available data (i.e., on the specific features of the detector, the source, and the observation), we find that high-quality reverberation measurements can improve upon constraints from the spectrum alone, even though most information is in the time-integrated profile. The key to using reverberation for testing the Kerr paradigm is the accumulation of sufficient line photons. Present setups surely oversimplify the picture. With current X-ray facilities, a good observation of a supermassive black hole can have $\sim 10^3$ photons in the iron line. With such a signal, even very deformed objects may be interpreted as Kerr BHs with a different spin. We instead consider an optimistic 10^5 photon data set, with a next-generation X-ray satellite in mind. With such data, we can perform a discerning test to check whether BH candidates are in fact the Kerr BHs of general relativity. Reverberation data can sharpen this test substantially.

The content of the Paper is as follows. In Section 2, we review the approach by which reverberation of the iron line is used to infer the geometry of the X-ray source and the BH spin in a Kerr background. In Section 3, we extend the formalism to non-Kerr backgrounds and show how reverberation can be used to test the actual nature of an astrophysical BH candidate. Section 4 demonstrates a preliminary quantitative analysis in which we compare iron line profiles and 2D transfer functions in Kerr and non-Kerr spacetimes to examine the possibility of distinguishing Kerr and non-Kerr BHs. Section 5 is devoted to a discussion of

[2]We note that the corona variability is unlikely described by actual "flares". There is indeed evidence that the emission of different regions is correlated on all time scales [69]. Nevertheless, such terminology is commonplace, and we employ the flare and response picture for its simplicity.

our results, with some attention to using iron line reverberation to test the Kerr metric and also the simplifications of our model that should be improved upon in future studies. Our summary and conclusions are reported in Section 6. Throughout the Paper, we use units in which $G_{\rm N} = c = 1$, so lengths and times are measured in units of M, the mass of the BH.

2 Iron line reverberation

2.1 The corona-disk model in lamppost geometry

Optically-bright AGNs are thought to host a central supermassive BH surrounded by an optically thick and geometrically thin accretion disk. In the disk, the mass flow is directed inward and the angular momentum flow is directed outward; the accretion disk radiates like a blackbody locally, or as a multi-color blackbody when integrated radially. In addition to this blackbody-like "thermal" component, the electromagnetic spectrum has other features which result from a hotter, usually optically-thin, electron cloud termed the "corona" which enshrouds the central disk and acts as a source of X-rays. This X-ray emitting corona is often approximated as a point source located on the axis of the accretion disk and just above the BH[3]. This arrangement is often referred to as a "lamppost geometry" and the full structure is termed the "corona-disk model" [73, 74]. The lamppost geometry requires a plasma of electrons very close to the BH and such a set-up may be realized in the case of the base of a jet. However, other geometries are possible, and an example is the family of "sandwich models" [75, 76]. Geometries different from the lamppost one are difficult to model using a fully general relativistic approach, because the number of free parameters is higher and the structure still ambiguous. However, some work has been done, see e.g. [77]. Here to illustrate these effects we consider the simplest case of lamppost geometry.

Different corona-disk models, consisting of a Kerr BH, an accretion disk, and an emitting source, have 2 characteristic parameters to be described. One is the spin parameter a_*, with $|a_*| \leq 1$ in order to describe a BH and not a naked singularity. The second one is the height of the source above the accretion disk, h, which is important for measuring time-dependent iron line signals. The standard framework to describe geometrically thin and optically thick accretion disks is the Novikov-Thorne model [78, 79], in which the disk is on the equatorial plane and the particles of the gas move on nearly geodesic circular orbits (i.e., Keplerian motion). The accretion disk is expected to have its inner edge at the radius of the ISCO, which in the Kerr background only depends on a_* and ranges from $r_{\rm ISCO} = 6\,M$ for a Schwarzschild BH to $r_{\rm ISCO} = M$ for an extremal Kerr BH with $a_* = 1$ and a corotating disk. In response of the illumination of the disk by the hot corona, fluorescent emission is produced at the disk's surface, termed a "reflection component" which is most distinguished by its prominent emission lines [80–82]. Here we will focus our attention only on the iron Kα line at ~ 6.4 keV, which is the strongest reflection line from BH candidates. In what follows, we set the emissivity index of the corona's intensity across the disk at $q = 3$ (unless stated otherwise), i.e., the coronal flux received by the disk is directly proportional to r^{-q}, where r is the disk's radius. We note that this approach oversimplifies the problem, because $q = 3$ is the asymptotic limit expected at large radii $r \gg M$, while at small radii near $r \approx h$, a proper reflection, lamppost model produces significant deviations [82, 83]. However, because our goal is to present a qualitative exploration of Kerr vs. non-Kerr geometries and given

[3] Although any true system must be physically extended and accordingly more complex, here we adopt the usual on-axis isotropic point source paradigm, which is theoretically clear and simple.

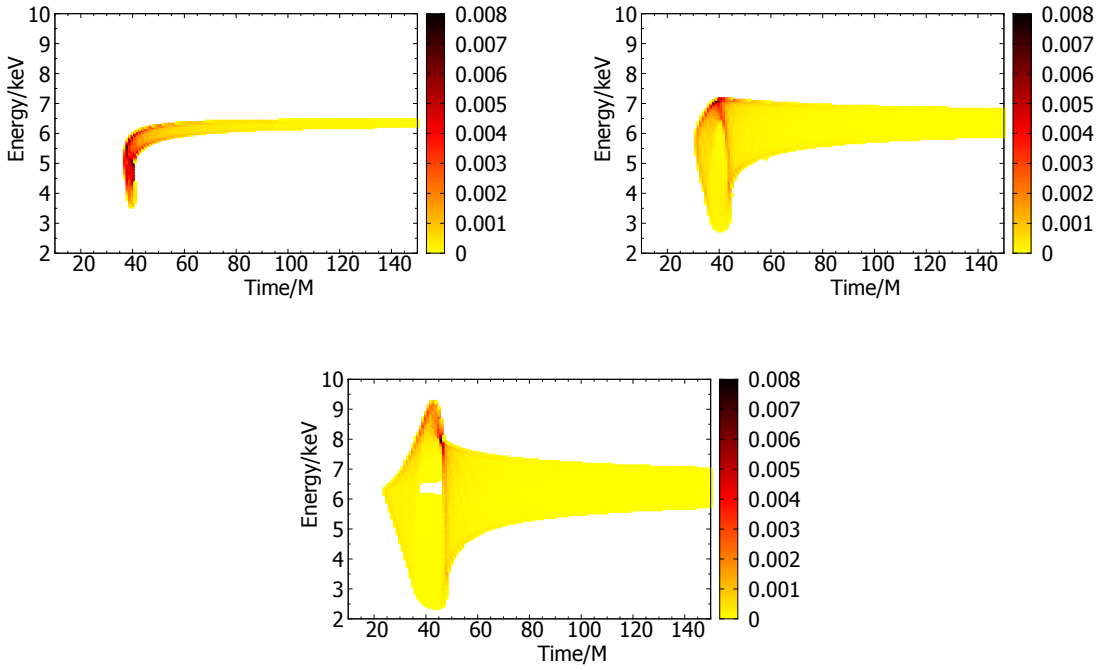

Figure 1. Transfer functions for a Kerr BH with spin parameter $a_* = 0.5$. The inclination angle is $i = 10°$ (top left panel), $i = 45°$ (top right panel), and $i = 80°$ (bottom panel). The height of the source is $h = 10\,M$ and the index of the intensity profile is $q = 3$. Flux in arbitrary units. See the text for more details.

that the precise coronal geometry is uncertain, we leave a more detailed treatment to future followup studies.

2.2 Line reverberation from an on-axis coronal flare

In the framework of the corona-disk model, "reverberation" refers to the iron line signal as a function of time in response to a δ-function like pulse of radiation from the X-ray primary source (i.e., the corona)[4]. The resulting line spectrum as a function of both time and across photon energy is called the 2D transfer function. As we show, the shape of this 2D transfer function is related to fundamental properties of the BH and also the system geometry. The transfer function becomes nonzero as the first photons reach the observer. Such photons are by construct those with the shortest path between the primary X-ray source, the disk, and the distant observer. The radial coordinate at which the shortest-path X-rays intercept the disk depends on the height of the source h. Likewise, the shortest path is dependent on the inclination of the disk with respect to the observer's line of sight, i. All other photons reaching the detector hit the disk at smaller and larger radii than that critical initial path, so they may have lower/higher energies as a result of a stronger/weaker gravitational redshift and different Doppler boosting. In the case of an almost face-on disk (small i), the situation is less complicated because the Doppler boosting is small and the gravitational redshift dominates. In this case, the transfer function exhibits two distinct branches (see the top left panel in Fig. 1): the high energy branch represents photons coming from further out in the disk, while

[4]We neglect the timescale over which X-rays are reprocessed in the disk atmosphere.

the low energy branch is produced by strongly redshifted photons from the innermost disk. The latter track terminates when photons from the ISCO reach the detector. At later times, the photon energy tends toward the value 6.4 keV, the rest-frame energy of iron Kα line, because at the larger radii at which these photons originate, the gravitational redshift is of diminishing importance.

2.3 The 2D transfer function for a Kerr background

In this paper, the calculations are done with an extension of the code described in Refs. [26, 30], which is based on a ray-tracing approach and photon trajectories are integrated backward in time from the plane of the distant observer to the emission point on the disk. The resulting 2D transfer functions for different viewing inclination angles are shown in Fig. 1. When the inclination angle of the observer is small, the Doppler boosting is subdominant and the gravitational redshift determines the shape of the transfer function. As the inclination angle increases, Doppler boosting becomes increasingly important. For photons hitting the disk at radii $r \approx 10 - 15\,M$, the Doppler blueshift can significantly exceed the gravitational redshift and produces a characteristic high-energy peak in the transfer function. Meanwhile, for photons hitting the disk at even larger radii, both gravitational redshift and Doppler boosting decrease in strength, with the net result that the photon energy is lower. The top left panel in Fig. 1 shows the transfer function for a low viewing angle, namely $i = 10°$, while the other two panels show broadened transfer functions corresponding to mid-range and nearly edge-on viewing angles, respectively $i = 45°$ and $i = 80°$. The higher the inclination angle, the more complicated the transfer function becomes. However, at late times the problem again simplifies, because only line emission from further out persists, and there the gravitational redshift becomes negligible and the width of the band around 6.4 keV is due to the Doppler redshift and blueshift caused by the orbital motion of the gas comprising the accretion disk. In fact, the width of the transfer function at late times has constraining power on the inclination angle of the disk. We note that the disk in many AGN systems may be warped, and in such a case the inclination angle of the inner part of the disk would not be the same as the inclination angle of the disk at its outer edge. The scales at which a warp from inner domain to outer are expected to be an order of magnitude or more larger than those relevant to the reverberation maps in this work (e.g., [84]), which probe scales $\lesssim 100M$, at which the Bardeen-Peterson effect is expected to keep the disk in strict alignment with the spin axis (but we also note there is still uncertainty in the true nature of AGN disks). At larger radii ($>> 10M$), the background metric has negligible effect and indeed this regime of the transfer function is essentially the same for Schwarzschild BHs and fast-rotating Kerr BHs (Figs. 2 and 3). However, the signal becomes fainter and fainter, so any measurement would accordingly become tenuous in strength.

The transfer functions for BHs with different spin parameters in the Kerr background differ at early times, since those photons originate in the strong-gravity region closest to the BH. The effect of spin at low inclination angles can be seen in the top left panel of Fig. 1 and in the left panels in Figs. 2 and 3. The low-energy, "red wing" of the transfer function depends significantly on the radius of the inner edge of the disk, which in the case of a geometrically thin and optically thick disk is thought to correspond with the ISCO radius (e.g., [85, 86]). For a Schwarzschild BH, the ISCO radius is at $r_{\rm ISCO} = 6\,M$ and the minimum photon energy is about 4 keV for $i = 10°$. As the spin parameter increases, the ISCO radius decreases and the minimum photon energy decreases. For $a_* = 0.95$ and $i = 10°$, the minimum photon energy of the emission line is lower than 2 keV and is off-scale for the left panel in Fig. 3.

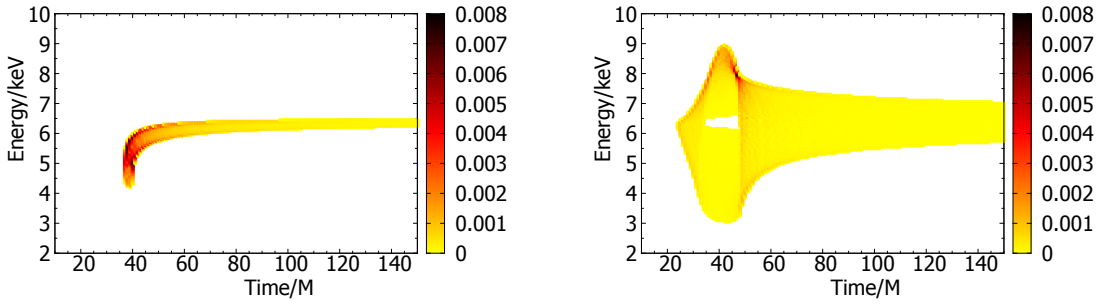

Figure 2. Transfer functions for a Schwarzschild BH ($a_* = 0$). The inclination angle is $i = 10°$ (left panel) and $i = 80°$ (right panel). The height of the source is $h = 10\,M$ and the emissivity index of the intensity profile is $q = 3$. Flux in arbitrary units. See the text for more details.

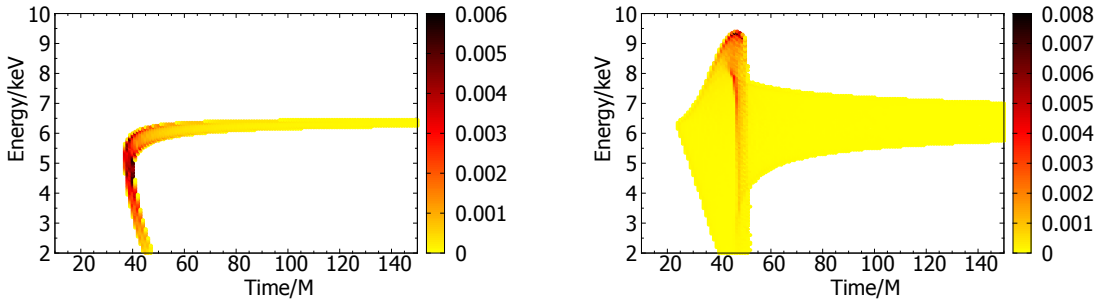

Figure 3. Transfer functions for a Kerr BH with spin parameter $a_* = 0.95$. The inclination angle is $i = 10°$ (left panel) and $i = 80°$ (right panel). The height of the source is $h = 10\,M$ and the index of the intensity profile is $q = 3$. Flux in arbitrary units. See the text for more details.

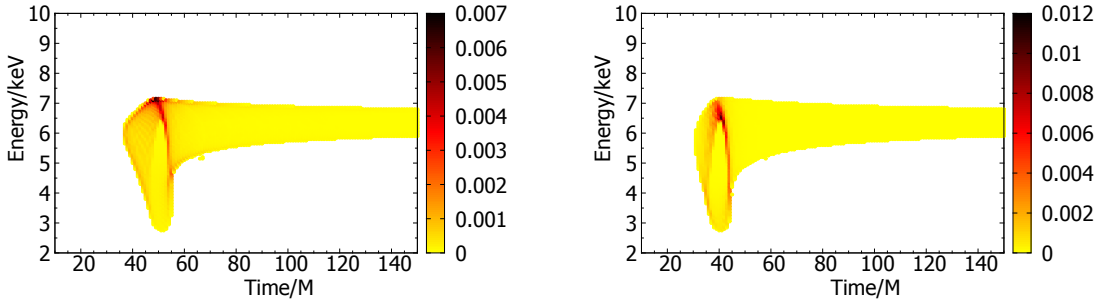

Figure 4. Transfer functions for a Kerr BH with spin parameter $a_* = 0.5$ and an inclination angle $i = 45°$. In the left panel, the height of the source is $h = 20\,M$ and the index of the intensity profile is $q = 3$. In the right panel, the height of the source is $h = 10\,M$ and the index of the intensity profile is $q = 6$. Flux in arbitrary units. See the text for more details.

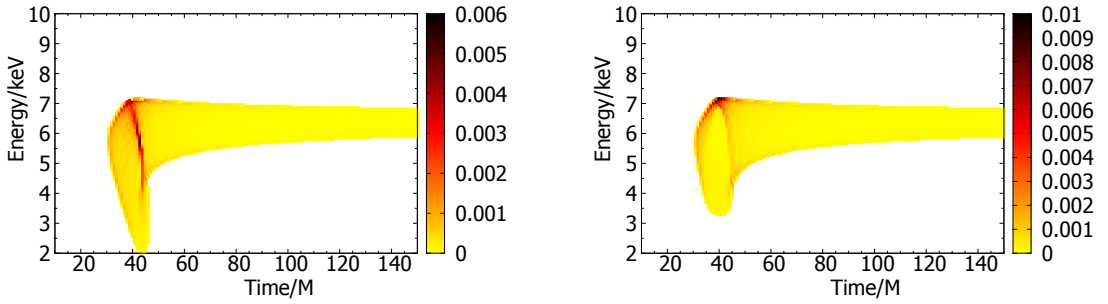

Figure 5. Transfer functions for Johannsen-Psaltis BHs with spin parameter $a_* = 0.5$ and deformation parameter $\epsilon_3 = 5$ (left panel) and $\epsilon_3 = -5$ (right panel). The height of the source is $h = 10\,M$ and the index of the intensity profile is $q = 3$. Flux in arbitrary units. See the text for more details.

The role of the source height is evident from the shift in the time of peak response when comparing the top right panel in Fig. 1 and the left panel in Fig. 4. The two transfer functions differ only in the corona's height; $h = 10\,M$ for the former, and $h = 20\,M$ for the latter. The source height affects the travel time of the photons from the X-ray source to the disk. If h increases, such a travel time increases as well, and therefore the distant observer detects a longer delay between the primary X-ray component that comes directly from the X-ray source and the reflection component from the disk. In the example shown in the left panel in Fig. 4 for a source with height $h = 20\,M$ and a viewing angle $i = 45°$, the transfer function begins at about $35\,M$, while the one in the right panel in Fig. 1 for $h = 10\,M$ begins at about $30\,M$. The height of the source affects also the time difference of the illumination of gas in the accretion disk at different radii. In the case of an on-axis point source in flat spacetime, the travel time from the source to the disk monotonically increases with the disk radius and the time difference between two different radii decreases as the height of the source increases, tending toward zero as $h \to \infty$. Because the observer's viewing angle affects the photon travel time from disk to observer, both the time difference between primary and reflection components, and also the shape of the transfer function depend non-trivially on the source height and viewing angle. However, the height of the source does not affect the photon energy, while the viewing angle does via the magnitude of Doppler boosting.

In flat spacetime, the reflected radiation from the accretion disk is given by

$$I \propto \frac{h}{(r^2 + h^2)^{\frac{3}{2}}}\,, \tag{2.1}$$

and without any relativistic effects, the intensity is related to the radius. A constant emissivity index is thus a simplification. In actuality, different radii on the accretion disk will have different emissivity indices. For larger radii, the emissivity index tends toward $q = 3$. We explore the effect of changing the emissivity index from $q = 3$ to $q = 6$, and note that the shape of the transfer function does not change at all, although the value of flux does, see the top right panel in Fig. 1 and the right panel in Fig. 4. Darker colors represent higher flux values. A steeper index causes the flux to fall off more rapidly with radius, and thus the later times at which those larger radii dominate the transfer function are correspondingly fainter for $q = 6$ than $q = 3$.

3 The 2D transfer function for non-Kerr backgrounds

In order to verify the Kerr nature of an astrophysical BH candidate, it is not enough to observe relativistic signatures absent in a Newtonian model and have a good fit to the BH's spectrum, because a non-Kerr BH may mimic a Kerr BH with a different spin parameter. Such a degeneracy appears to be a common feature of non-Kerr structures. In order to quantify possible deviations from the Kerr background, we have to consider a general BH metric specified by a mass M, spin parameter a, and additional free parameters (usually called deformation parameters) that must recover the Kerr solution as they vanish. The calculations of the theoretical predictions of the BH spectrum is performed within this more general spacetime, and the comparison between predictions and observations are used to measure the value of all the parameters of the background metric. The Kerr BH hypothesis is verified if observations agree with vanishing deformation parameters.

In principle, the test-metric should be sufficiently general that, for arbitrary values of the deformation parameters, it would be possible to recover any BH solution in any theory of gravity. However, at present there is no general framework that can take arbitrary deviations from the Kerr metric into account. In addition, there is a strong correlation between the measured spin parameter and deformation parameters measuring departure from the Kerr solution. Because of this, current observations are severely challenged in assessing even one deformation parameter. Therefore, we restrict our attention to the *simplest* scenario, in which the object is allowed to be either more oblate or more prolate than a Kerr BH with the same spin and its departure from the Kerr solution is regulated by a single deformation parameter. We accordingly adopt the simplest version of the Johannsen-Psaltis metric which employs one deformation parameter [87]. In Boyer-Lindquist coordinates, the line element reads

$$\begin{aligned} ds^2 = &-\left(1-\frac{2Mr}{\Sigma}\right)(1+h)\,dt^2 - \frac{4aMr\sin^2\theta}{\Sigma}(1+h)\,dtd\phi + \frac{\Sigma\,(1+h)}{\Delta+a^2h\sin^2\theta}dr^2 + \\ &+\Sigma d\theta^2 + \left[\left(r^2+a^2+\frac{2a^2Mr\sin^2\theta}{\Sigma}\right)\sin^2\theta + \frac{a^2(\Sigma+2Mr)\sin^4\theta}{\Sigma}h\right]d\phi^2\,, \end{aligned} \tag{3.1}$$

where $\Sigma = r^2 + a^2\cos^2\theta$, $\Delta = r^2 - 2Mr + a^2$, and

$$h = \frac{\epsilon_3 M^3 r}{\Sigma^2}\,. \tag{3.2}$$

ϵ_3 is the deformation parameter. The compact object is more prolate (oblate) than a Kerr BH for $\epsilon_3 > 0$ ($\epsilon_3 < 0$); when $\epsilon_3 = 0$, we exactly recover the Kerr solution.

The reverberation calculations for a Kerr background as treated in the previous section can be quite naturally extended to Johannsen-Psaltis spacetime. Now, the parameters of the spacetime geometry are a_* and ϵ_3 (M simply sets the scale of the system but otherwise factors out of any calculation). Fig. 5 shows the transfer functions for BHs with spin parameter $a_* = 0.5$ and non-vanishing ϵ_3. They can be compared with the transfer function in the top right panel in Fig. 1, where the only difference is that for Fig. 1 the deformation parameter is zero; that is, the object is a Kerr BH. The most important difference between these transfer functions is that ϵ_3 affects the ISCO radius and thus the minimum photon energy. For $\epsilon_3 = 5$ (left panel in Fig. 5), the inner edge of the disk is closer to the BH than in the Kerr solution, so photons experience a stronger gravitational redshift and the transfer function extends to energies lower than 2 keV. For $\epsilon_3 = -5$ (right panel in Fig. 5), the object is more oblate than its Kerr counterpart, so the gravitational force on the equatorial plane is

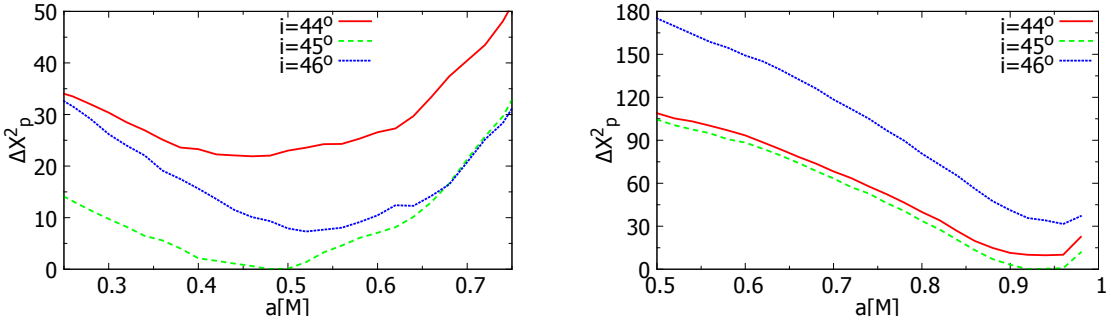

Figure 6. Left panel: The change in $\chi^2_{\rm p}$ compared to its minimum; $\chi^2_{\rm p} \approx N\mathcal{L}_{\rm p}$ with $N = 10^3$ from the comparison of the iron line profile of a Kerr BH with spin parameter $a'_* = 0.5$ and inclination angle $i' = 45°$ and the iron line profile of Kerr BHs with spin parameter a_* and inclination angle $i = 44°$, $45°$, and $46°$. Right panel: as in the left panel with a reference iron line profile of a Kerr BH with spin parameter $a'_* = 0.95$ and inclination angle $i' = 45°$. The index of the intensity function is always assumed to be $q = q' = 3$. See the text for more details.

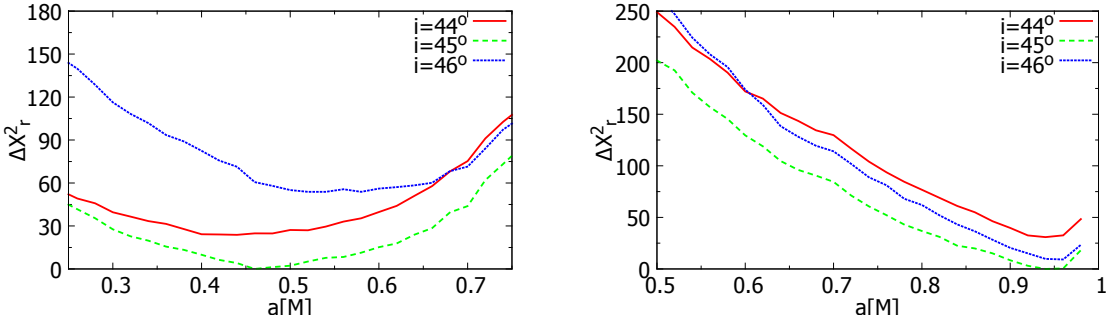

Figure 7. Left panel: Change in $\chi^2_{\rm r}$ compared to its minimum; $\chi^2_{\rm r} \approx N\mathcal{L}_{\rm r}$ with $N = 10^3$ from the comparison of the 2D transfer function of a Kerr BH with spin parameter $a'_* = 0.5$ and inclination angle $i' = 45°$ and the 2D transfer function of Kerr BHs with spin parameter a_* and inclination angle $i = 44°$, $45°$, and $46°$. The time range of the 2D transfer function is $[0, 300\,M]$. Right panel: as in the left panel with a reference 2D transfer function of a Kerr BH with spin parameter $a'_* = 0.95$ and inclination angle $i' = 45°$. The index of the intensity function is always assumed to be $q = q' = 3$ and the height of the source $h = h' = 10\,M$. See the text for more details.

stronger and the ISCO radius is larger. In this spacetime, photons coming from the inner part of the accretion disk are less affected by the gravitational redshift as compared to cases with $\epsilon_3 = 5$ or $\epsilon_3 = 0$, so the red wing of the 2D transfer function is less extended. However, the transfer function is imprinted with more information about the spacetime geometry. As a result, different backgrounds experience different Doppler boosting, different light bending, and different time delays. All these relativistic effects are encoded in the 2D transfer function.

4 Comparison of Kerr and non-Kerr models

Now we want to compare line profiles and reverberation transfer functions of Kerr and non-Kerr models. Let us consider a primary model for which the BH has spin parameter a_*, deformation parameter ϵ_3, the disk is observed from an inclination angle i, the emissivity index is q and the height of the on-axis X-ray source is h. Here we employ a single inclination

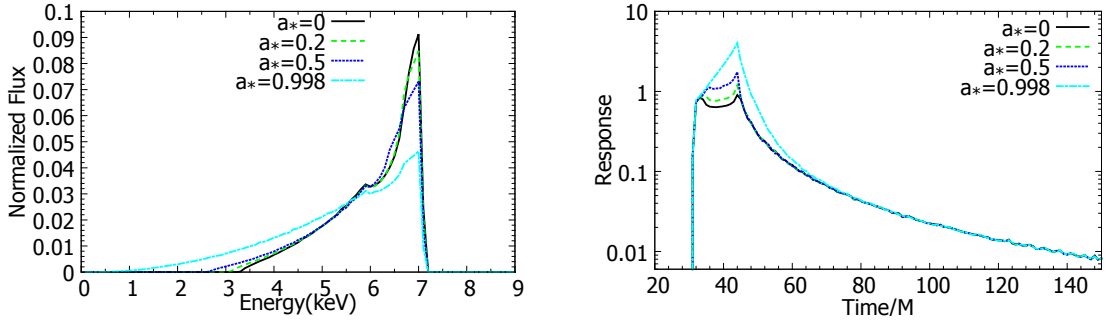

Figure 8. Left panel: iron line profile (time-integrated 2D transfer function) for Kerr BHs with spin $a_* = 0$, 0.2, 0.5, and 0.998, an inclination angle $i = 45°$, and an emissivity index $q = 3$. Right panel: as in the left panel for the response function (energy-integrated 2D transfer function) and a source height $h = 10\,M$. See the text for more details.

angle of the disk, namely we do not consider the possibility that the disk is warped at these scales. We use the notation

$$n_j = n(a_*, \epsilon_3, i, q) \tag{4.1}$$

to indicate the photon flux number density in the energy bin $[E_j, E_j + \Delta E]$ of the iron line profile. Similarly, for the 2D transfer function, we employ the notation

$$n_{jk} = n(a_*, \epsilon_3, i, q, h) \tag{4.2}$$

for the photon flux number density in the energy bin $[E_j, E_j + \Delta E]$ and in the time bin $[t_k, t_k + \Delta t_k]$. We take a secondary model to be compared with the primary for which the BH has spin parameter a'_*, deformation parameter ϵ'_3, the disk is observed from an inclination angle i', the emissivity index is q' and the height of the on-axis X-ray source is h'. The secondary model line profile and transfer function intensities are expressed, respectively, as $n'_j = n(a'_*, \epsilon'_3, i', q')$ and $n'_{jk} = n(a'_*, \epsilon'_3, i', q', h')$. We introduce the normalized (negative) log-likelihood $\mathcal{L}_\mathrm{p}$ and $\mathcal{L}_\mathrm{r}$ for means of comparison between the primed and unprimed iron line *profiles* and 2D *reverberation* transfer functions. We adopt notations of p and r to emphasize which situation is being considered:

$$\mathcal{L}_\mathrm{p} = \frac{1}{\sum_j n_j} \left[\sum_j \frac{\left(n_j - \alpha_\mathrm{p} n'_j \right)^2}{n_j} \right] , \tag{4.3}$$

$$\mathcal{L}_\mathrm{r} = \frac{1}{\sum_{j,k} n_{jk}} \left[\sum_{j,k} \frac{\left(n_{jk} - \alpha_\mathrm{r} n'_{jk} \right)^2}{n_{jk}} \right] , \tag{4.4}$$

where $\alpha_\mathrm{p,r}$ is chosen to minimize $\mathcal{L}_\mathrm{p,r}$, namely

$$\alpha_\mathrm{p} = \frac{\sum_j n'_j}{\sum_j n'^2_j / n_j} , \quad \alpha_\mathrm{r} = \frac{\sum_{j,k} n'_{jk}}{\sum_{j,k} n'^2_{jk} / n_{jk}} . \tag{4.5}$$

The corresponding chi-square is, respectively, $\chi^2_\mathrm{p} \approx N\mathcal{L}_\mathrm{p}$ and $\chi^2_\mathrm{r} \approx N\mathcal{L}_\mathrm{r}$, where N is the number of detected photons. Given a mission sensitivity, we can estimate which features

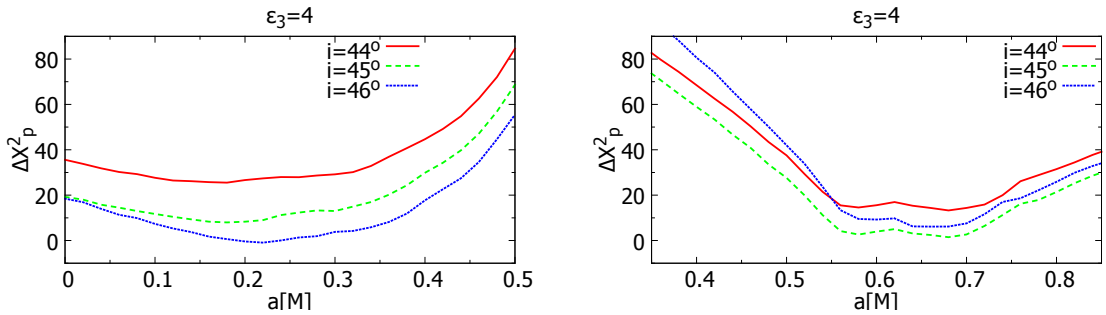

Figure 9. Left panel: Change in $\chi^2_{\rm p}$ compared to its minimum; $\chi^2_{\rm p} \approx N\mathcal{L}_{\rm p}$ with $N = 10^3$ from the comparison of the iron line profile of a Kerr BH with spin parameter $a'_* = 0.5$ and inclination angle $i' = 45°$ and the iron line profile of Johannsen-Psaltis BHs with spin parameter a_*, deformation parameter $\epsilon_3 = 4$, and inclination angle $i = 44°$, $45°$, and $46°$. Right panel: as in the left panel with a reference iron line profile of a Kerr BH with spin parameter $a'_* = 0.95$. The index of the intensity function is always assumed to be $q = q' = 3$. See the text for more details.

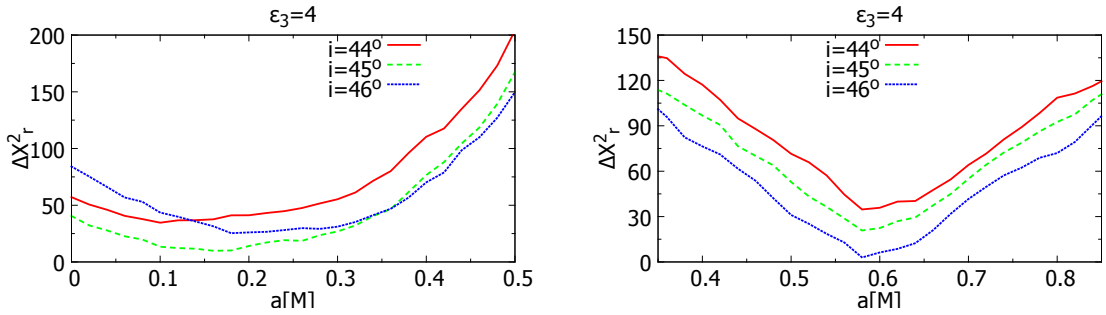

Figure 10. Left panel: Change in $\chi^2_{\rm r}$ compared to its minimum; $\chi^2_{\rm r} \approx N\mathcal{L}_{\rm r}$ with $N = 10^3$ from the comparison of the 2D transfer function of a Kerr BH with spin parameter $a'_* = 0.5$ and inclination angle $i' = 45°$ and the 2D transfer function of Johannsen-Psaltis BHs with spin parameter a_*, deformation parameter $\epsilon_3 = 4$, and inclination angle $i = 44°$, $45°$, and $46°$. The time range of the 2D transfer function is $[0, 300\,M]$. Right panel: as in the left panel with a reference 2D transfer function of a Kerr BH with spin parameter $a'_* = 0.95$. The index of the intensity function is always assumed to be $q = q' = 3$ and the height of the source $h = h' = 10\,M$. See the text for more details.

can potentially be distinguished and at which level of confidence. In what follows, we use either $N = 10^3$, corresponding to a high-quality observation today, and $N = 10^5$, which is an optimistic benchmark for a quality observation with a next generation of X-ray satellite. Moreover, we adopt $\Delta E = 0.05$ keV and $\Delta t = M$ (e.g., for $M = 10^6\,M_\odot$, $\Delta t \approx 5$ s). M is also a model parameter in the transfer function, but its value would often be obtained externally using optical data (e.g., [88]). Moreover, in a fit it should be correlated with the height of the source, in the sense that the height and mass are degenerate for a given lag [89], but not with the parameters of the spacetime geometry close to the BH.

We simulate observations of iron lines from our models for an arbitrary N photons, incorporating Poisson noise, and treat the simulation as if it were data. To this end, our analysis employs standard techniques, consisting of grouping the data to a minimum of 10 counts per bin. Because of these observation-mimicking procedures, the relationship between χ^2 and $N\mathcal{L}$ is only approximate (it becomes exact in the limit of high counts). Here we adopt

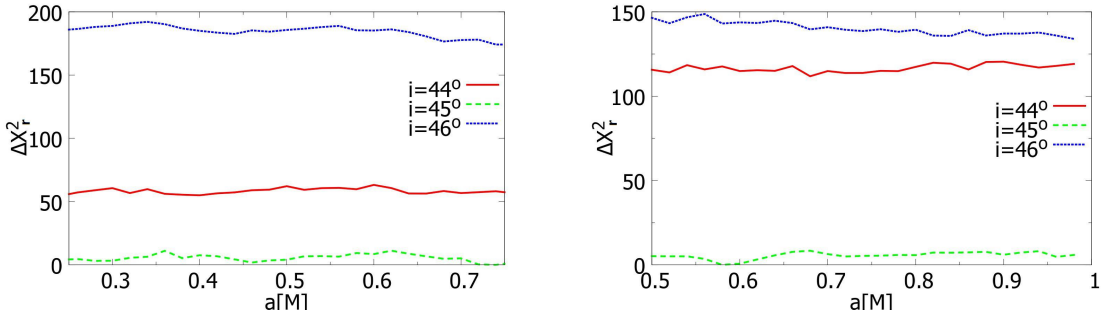

Figure 11. Left panel: As in Fig. 7, but for the time range $[100\,M, 300\,M]$ which contains $N = 5000$. See the text for more details.

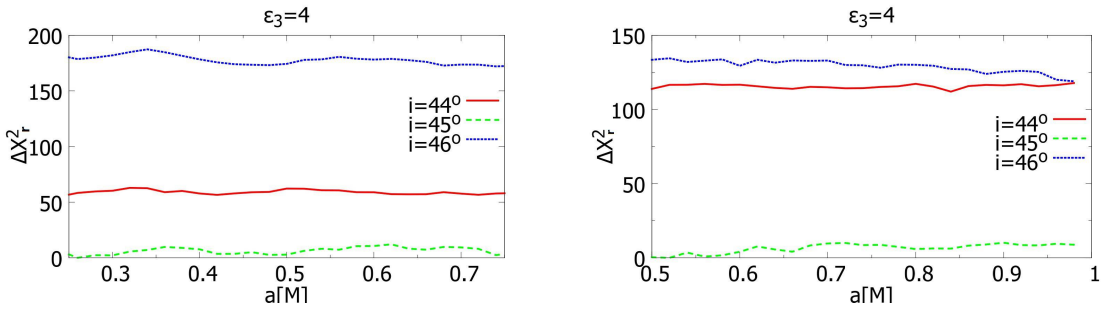

Figure 12. Left panel: As in Fig. 10, but the time range $[100\,M, 300\,M]$ which contains $N = 5000$. See the text for more details.

a minimum of 10 counts per bin which achieves a 3-sigma significance per bin. We note that this choice is arbitrary; there are other reasonable choices of binning; however, this is of minor consequence and has no impact on our results.

4.1 Role of the model parameters

In this Paper, our emphasis is on correlation between the spin measurement, deformation parameter, and the viewing angle. Although other parameter correlations may also be explored, we find that the spin and viewing angle are more correlated with the deformation parameter measurement than e.g., the emissivity index or the height of the source. While in this *exploratory* work we maintain a more narrow focus, we note that followup work seeking precise spin or deformation parameter determination should fully examine degeneracy between all model parameters.

In Fig. 6, we compare the *time-integrated* iron line profiles of Kerr BHs with spin parameter $a'_* = 0.5$ (left panel) and $a'_* = 0.95$ (right panel) observed with an inclination angle $i' = 45°$ and the iron line profiles of Kerr BHs with spin parameter a_* (x axis) and observed with an inclination angle $i = 44°$ (red solid line), $45°$ (green dashed line), and $46°$ (blue dotted line). The emissivity index is always assumed to be $q = q' = 3$. $\chi^2_{\rm p}$ is calculated with $N = 10^3$. In Fig. 7, we show $\chi^2_{\rm r}$, the chi-square obtained from the comparison of the 2D

transfer functions. Here the time interval is $[0, 300\ M]$ and N is still 10^3. Figs. 6 and 7 suggest that reverberation mapping can provide stronger constraints on the spacetime geometry, the improvement is significant but still modest, i.e., most of the information is already in the iron line profile. This has elsewhere been established for a pure Kerr model in Ref. [89]. Fig. 8 shows the iron line profile (time-integrated 2D transfer function, left panel) and the response function (energy-integrated 2D transfer function, right panel) of BHs with different spin parameters.

In the same spirit, we can compare iron line profiles and 2D transfer functions of Kerr and Johannsen-Psaltis BHs. This is done, respectively, in Fig. 9 and Fig. 10. In these plots, the reference spectra are again Kerr BHs with $a'_* = 0.5$ (left panels) and $a'_* = 0.95$ (right panels), with the same inclination angle $i' = 45°$, emissivity index $q' = 3$, and height of the source $h = 10\,M$, but they are compared to objects in the Johannsen-Psaltis metric with $\epsilon_3 = 4$. In these simulations, we have assumed $N = 10^3$. The minimum of $\chi^2_{\rm p}$ is not always for $i = i'$. This is, in part, because there is a correlation between the spin, the deformation parameter, and the inclination angle; that is, a non-Kerr object observed from a certain inclination angle may be interpreted as a Kerr BH with a different spin parameter and observed from a different inclination angle. This is exacerbated by the "low" photon count $N = 10^3$.

The advantages of the 2D transfer function is that we can potentially measure effects from different radii, which is impossible using the time-averaged signal. However, a higher signal is necessary to employ this technique. As one clear benefit, reverberation mapping can accurately pick out the inclination angle of the disk from the photons detected at later time, coming from larger radii. The photons detected in the time interval $[100\,M, 300\,M]$ are about 5% of the total photons in $[0, 300\,M]$. For $N = 10^3$, the mere ~ 50 photons are insufficient signal. For $N = 10^5$, the yield is about 5000 photons which provide a constraint on the inclination angle which is independent of the background geometry, as shown in Figs. 11 and 12. We note that the curves demonstrate how this late-time signal contains essentially no information on the spin. As we will show in the next subsection, even the time-integrated iron line profile with $N = 10^5$ can correctly select the right inclination angle. However, the determination of the inclination angle from late time photons can be considered robust, as it is independent of the reflection properties at small radii.

The impact of the emissivity index on the iron line profile and the 2D transfer function is shown, respectively, in Fig. 13 and Fig. 14. For the sake of simplicity, we here fix the inclination angle and the height of the source. It is important to note that one can explicitly link the height h to $q(r)$, which requires more detailed modeling, e.g., [83]. However, this is beyond the scope of this exploratory work, in which we treat q as a constant for simplicity. The 2D transfer function can far better distinguish the effects of the spin from those of the emissivity index with respect to the time-integrated spectrum: the curves for which emissivity index differs from the reference model are well above the curve with the correct emissivity index across a wide spin range. By contrast, this is not the case for the time-integrated spectra, for which models with erroneous emissivity indexes but spins close to the reference value produce superior fits than the models with correct emissivity indexes but vastly different spins. As shown in Ref. [30], unlike inclination angle, the emissivity index constraint is very weakly correlated with the estimate of the deformation parameter from the iron line profile. Such a result can be qualitatively understood by noting that the deformation parameter affects the redward extent of the low-energy tail (which relates to the inner edge of the disk and the relativistic effects there) as well as the position of the high-energy peak

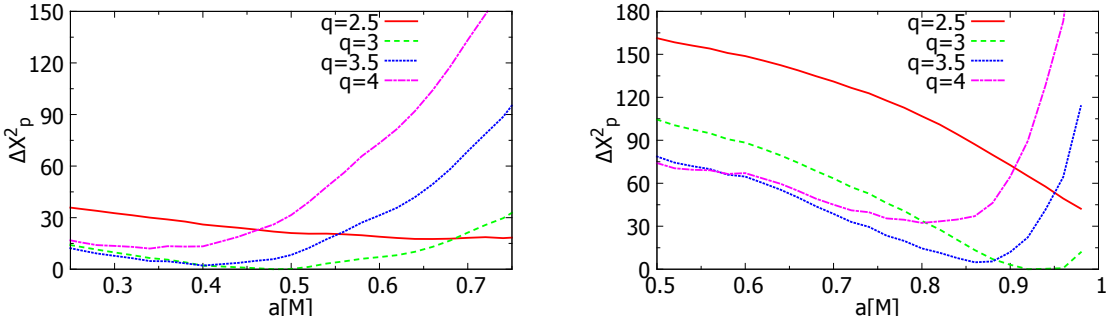

Figure 13. Left panel: Change in $\chi^2_{\rm p}$ compared to its minimum; $\chi^2_{\rm p} \approx N\mathcal{L}_{\rm p}$ with $N = 10^3$ from a comparison of the iron line profile of a Kerr BH with spin parameter $a'_* = 0.5$ and emissivity index $q' = 3$ versus a set of Kerr BHs with emissivity indexes $q = 2.5$, 3, 3.5, and 4, as a function of spin a_*. Right panel: as in the left panel but with a reference Kerr BH with spin parameter $a'_* = 0.95$. The inclination angle has been fixed to 45° for all models. See the text for more details.

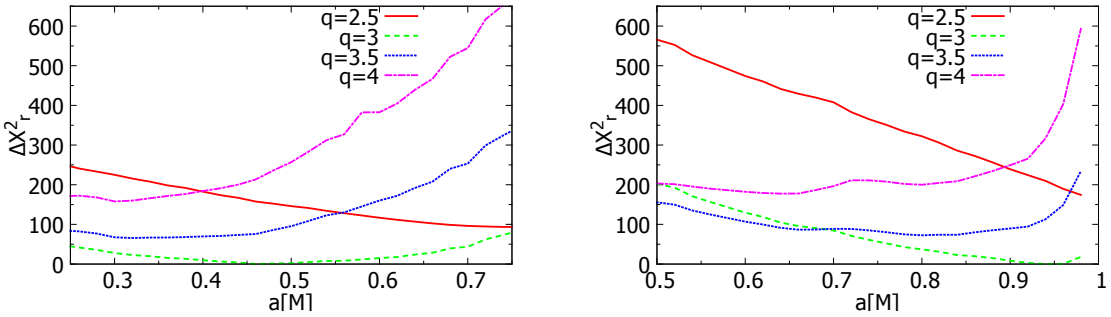

Figure 14. Left panel: Change in $\chi^2_{\rm r}$ compared to its minimum; $\chi^2_{\rm r} \approx N\mathcal{L}_{\rm r}$ with $N = 10^3$ from a comparison of the 2D transfer function of a Kerr BH with spin parameter $a'_* = 0.5$ and emissivity index $q' = 3$ versus a set of Kerr BHs with emissivity indexes $q = 2.5$, 3, 3.5, and 4, as a function of spin a_*. The time range of the 2D transfer function is $[0, 300\,M]$. Right panel: as in the left panel but with a reference Kerr BH with spin parameter $a'_* = 0.95$. The inclination angle has been fixed to 45° and height of the source taken as $10\,M$ for all models. See the text for more details.

(which is produced by the Doppler boosting at larger radii, where the gravitational redshift is milder but the angular frequency of the orbit still high). By contrast, the emissivity index alters the relative flux received by each region of the disk. It cannot move to lower or higher energies the position of the low-energy tail or of the most blueshifted photons. In light of this and given the superior capability of reverberation mapping to distinguish the effects of spin from emissivity index, we argue that the correlation between the measurements of the deformation parameter and of the emissivity index from the 2D transfer function is quite weak and can be reasonably neglected compared to the sizable correlation with the viewing angle i.

Lastly, we consider the role of the source height in Fig. 15. In this case we cannot compare the iron line profile with reverberation mapping because, in the prescription adopted, the former contains no information about this parameter. As discussed in [89], the measurement of the height of the source and the measurement of the mass are degenerate for a given lag, in cases for which M is not independently known. However, because M is often externally constrained and given also that there is no significant correlation between M with

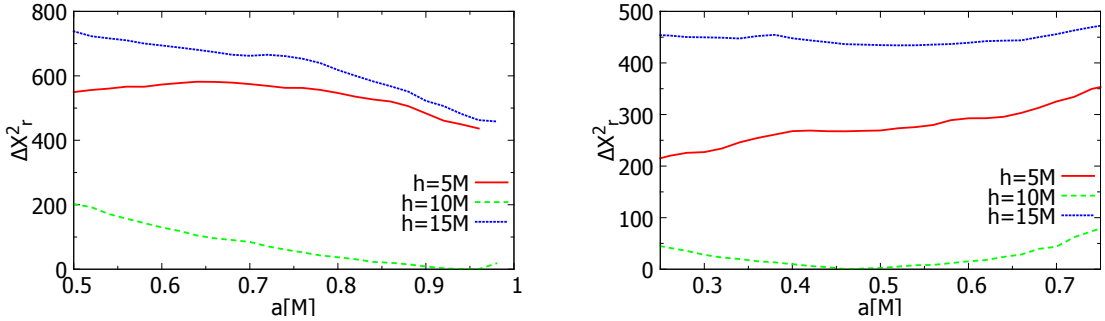

Figure 15. Left panel: Change in $\chi^2_{\rm r}$ compared to its minimum; $\chi^2_{\rm r} \approx N\mathcal{L}_{\rm r}$ with $N = 10^3$ from a comparison of the 2D transfer function of a Kerr BH with spin parameter $a'_* = 0.5$ and a lamppost corona height $h' = 10\,M$ versus a set of Kerr BHs with a range of corona height $h = 5\,M$, $10\,M$, and $15\,M$, as a function of spin a_*. The time range of the 2D transfer function is $[0, 300\,M]$. Right panel: as in the left panel but with a reference Kerr BH with spin parameter $a'_* = 0.95$. The inclination angle is $i = i' = 45^\circ$ and emissivity index is $q = q' = 3$. See the text for more details.

the spacetime geometry close to the putative BH, we keep M fixed in our analysis for purposes of examining possible tests of the Kerr metric. A detailed consideration of the effect of keeping M free is left to other work. From Fig. 15 it seems that reverberation mapping is quite sensitive to the exact value of the height of the source. The models with $h = 5\ M$ and $15\ M$ have a $\Delta\chi^2$ significantly larger than any model with the correct height. Such a constraining power can be presumably quite useful in models in which the index emissivity $q(r)$ depends on the height h [83].

4.2 A non-Kerr black hole example

Thus far, we have broadly explored a select few correlations within a large multi-dimensional parameter space. We now more carefully consider one particular non-Kerr template model to assess whether we can constrain the deformation parameter and whether we can distinguish our object from a Kerr BH. We assume a Johannsen-Psaltis BH with spin parameter $a'_* = 0.25$ and deformation parameter $\epsilon'_3 = 8$. We similarly adopt an inclination angle $i' = 45^\circ$, an emissivity index $q' = 3$, and a height for the X-ray source $h' = 10\,M$, and use this as our reference model.

First, we consider the time-integrated line profile. Fig. 16 shows contours of $\Delta\chi^2_{\rm p}$ with $N = 10^3$ (top panels) and 10^5 (bottom panels). In the left panels, we make the simplifying assumption that the inclination angle and the emissivity index are known, i.e., we set $i = i'$ and $q = q'$. In the right panels, i is instead treated as a fit parameter. To isolate the importance of inclination, we again adopt $q = q'$. However, such an approach is motivated given the weak correlation between q and the geometry parameters, as discussed above. We note a few important points. First, for $N = 10^3$ if the inclination angle were known then the iron line spectrum could on its own establish the non-vanishing deformation parameter of our template robustly (top left panel in Fig. 16). However, the power of this constraint is substantially reduced when allowing inclination to vary. Second, for $N = 10^5$ we have a substantial improvement in the measurement quality allowing for strong testing of the Kerr metric (bottom panels in Fig. 16). Third, in the case of $N = 10^5$ we break the degeneracy arising from the inclination angle.

A parallel analysis has been performed but considering the full reverberation mapping signal, as opposed to the integrated line profile. The results are shown in Fig. 17, for $N = 10^3$

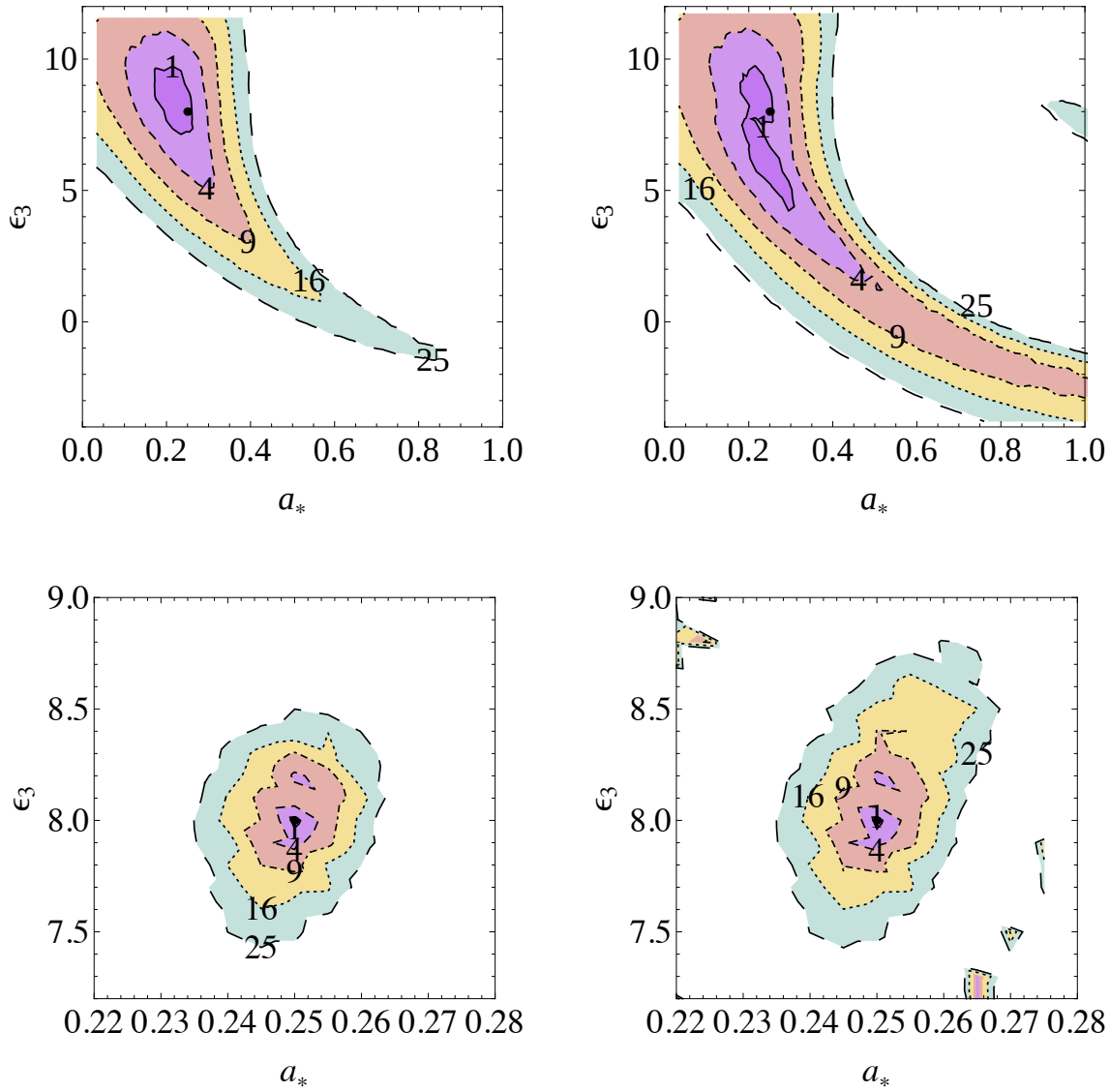

Figure 16. Top panels: $\Delta\chi^2_{\rm p}$ contours with $N = 10^3$ from the comparison of the iron line profile of a Johannsen-Psaltis BH with a spin parameter $a'_* = 0.25$, deformation parameter $\epsilon'_3 = 8$, and an inclination of $i' = 45°$ versus a set of Johannsen-Psaltis BHs with spin parameters a_* (x axis) and deformation parameters ϵ_3 (y axis). In the left panel, all models use an inclination angle $i' = i = 45°$. In the right panel, i is free in the fit. For the sake of simplicity, the emissivity index is fixed to $q' = q = 3$. Bottom panels: as in the top panels with $i = 45°$ (left panel) and i free (right panel) for $N = 10^5$. See the text for more details.

(top panels) and $N = 10^5$ (bottom panels). As in Fig. 16, for the left panels, $i = i'$, while in the right panels i is treated as a fit parameter and we have minimized $\chi^2_{\rm r}$ across all inclination values. As discussed above, we have adopted $q = q' = 3$, $h = h' = 10\,M$, and the time range is $[0, 300\,M]$. Reverberation mapping is more powerful than the time-averaged iron line profile, and the difference is most pronounced for the constraint on spin. If we compare the top right panels in Figs. 16 and 17, the allowed regions are narrower in spin for the case of reverberation mapping, but it is difficult to constrain a Kerr deviation with $N = 10^3$ photons. But we find the situation is much improved with sufficiently high signal. An observation with $N = 10^5$

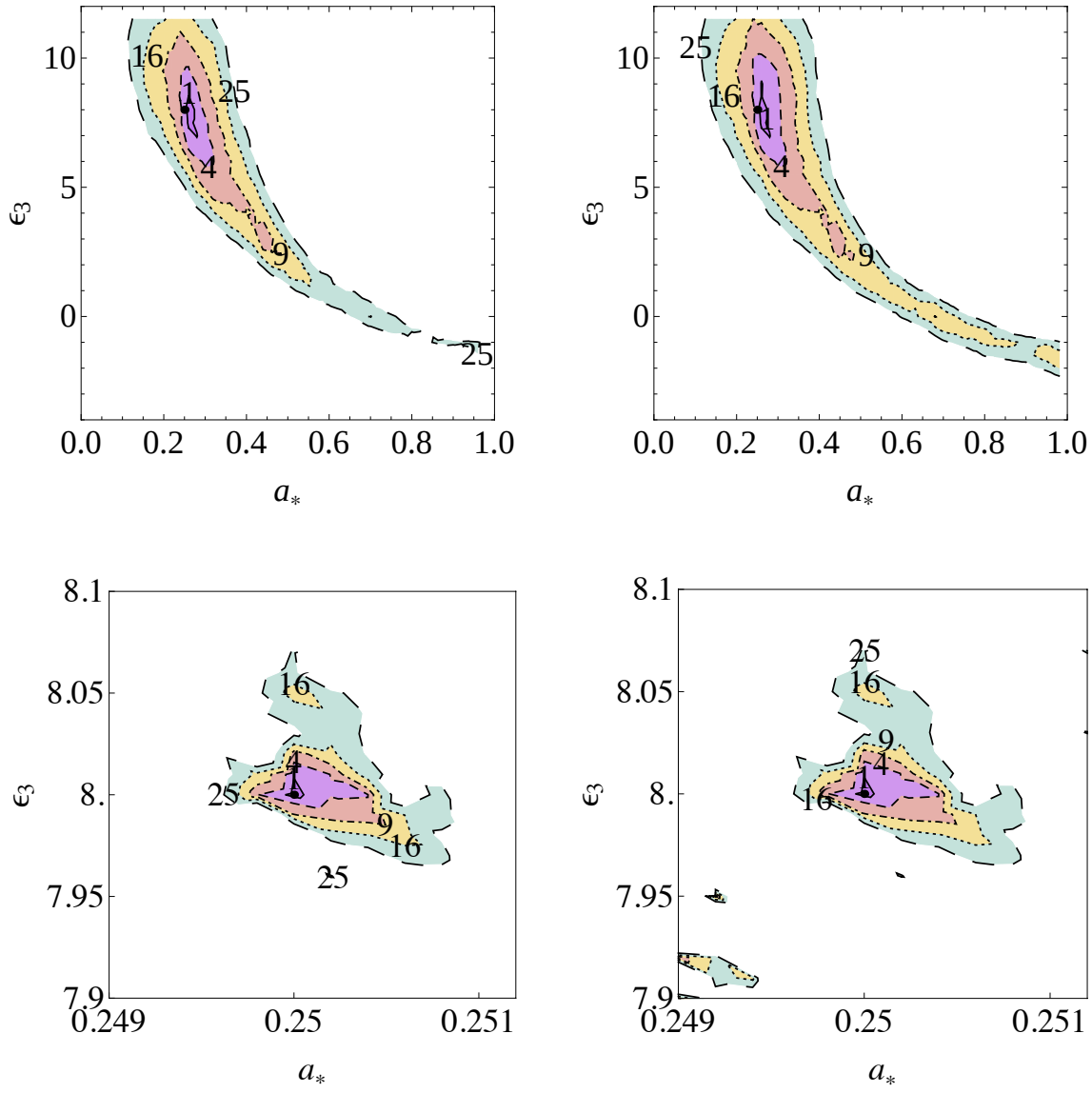

Figure 17. Top panels: $\Delta\chi^2_{\rm r}$ contours with $N = 10^3$ from the comparison of the 2D transfer function of a Johannsen-Psaltis BH with a spin parameter $a'_* = 0.25$, deformation parameter $\epsilon'_3 = 8$, and an inclination of $i' = 45°$ versus a set of Johannsen-Psaltis BHs with spin parameters a_* (x axis) and deformation parameters ϵ_3 (y axis). In the left panel, all models use an inclination angle $i' = i = 45°$. In the right panel, i is free in the fit. For the sake of simplicity, the emissivity index is fixed to $q' = q = 3$ and the source height is $h' = h = 10\,M$. The time range of the 2D transfer function is $[0, 300\,M]$. Bottom panels: as in the top panels with $i = 45°$ (left panel) and i free (right panel) for $N = 10^5$. See the text for more details.

photons can readily distinguish a Kerr BH from one with $\epsilon_3 = 8$ from the integrated spectrum alone. However, the time information improves the quality of constraint by roughly an order of magnitude, from $\Delta\epsilon_3 \sim 1$ (profile), to $\Delta\epsilon_3 \sim 0.1$ (reverberation). This enormous gain means a much more potent constraint on deviations from Kerr is enabled by additional time information, but clearly also requires appreciable signal to make the difference.

While here we have provided just a single example with a large value of the deformation

parameter, the behavior of the metric with respect to ϵ_3 is relatively smooth. As a crude estimate, we can imagine the constraint for a different value of the spin and the deformation parameter of the reference model simply adopting the uncertainty on a_* and ϵ_3 shown in Figs. 16 and 17.

5 Discussion

In the previous section, we compared a number of Kerr and non-Kerr models to determine if and how reverberation measurements provide extra information about the nature of BH candidates compared to the readily available measurements of time-integrated iron line spectra. Within our simplified analysis, we have used $\chi^2_{\rm p} \approx N\mathcal{L}_{\rm p}$ and $\chi^2_{\rm r} \approx N\mathcal{L}_{\rm r}$ to quantify the level of similarity between iron line profiles and between 2D reverberation transfer functions for different models. Here N is the total photon number and $\mathcal{L}_{\rm p,r}$ is the log-likelihood defined in Eqs. (4.3) and (4.4). In our figures, we have assumed either $N = 10^3$ or $N = 10^5$. At first approximation, our results can be rescaled for a different photon number, but the fact we have included the photon noise and required a minimum of 10 photons per bin introduces some deviations from an exact scaling.

Although we have adopted several simplifications, our results indicate that an accurate measurement of the 2D transfer function has advantages for testing the Kerr nature of astrophysical BH candidates compared to the analysis of the iron line profile alone. However, the difference is only substantial at high photon count; $N = 10^5$ photons can strongly constrain the Kerr metric even in the case of a time-integrated measurement. It should be clear that actually the constraints shown in the bottom panels in Fig. 16 and 17 are not realistic as at a certain point systematics effects due to a simplified model become important. Despite that, from Fig. 16 and 17 it is clear that current iron line data cannot rule out even large deviations from the Kerr solution, even in the best cases. The possibility of future detections with a large number of photons in the iron line can provide interesting constraints and test the Kerr paradigm. Much of the information on the spacetime geometry is already encoded in the spectrum alone (e.g., [89]). However, reverberation mapping is potentially a more reliable technique to understand the systematics. With added time information, we can distinguish photons emitted at different radii and therefore affected in a different way by relativistic effects. In the case of the time-integrated iron line, photons emitted from different radii can sum up in the same energy bin and so added the information is lost. For example, a background independent estimate of the inclination angle from the late time 2D transfer function is a robustly determined quality.

Lastly, we note that our theoretical model, and this investigation, employ numerous simplifications. While these simplifications are reasonable for an exploration, followup study using a more thorough treatment of the various model degeneracies is necessary before a serious observational campaign for testing the Kerr BH hypothesis would be viable. There are many assumptions made here, and even elsewhere in iron-line spectral modeling that should be improved upon (and indeed, are the subject of ongoing work). For example, here the flaring region has been approximated by an on-axis point-like source. A more realistic model should be able to take into account multiple locations, extended geometry, or motion of the illuminating X-ray source [90]. The emissivity function has been modeled as a power law $\sim 1/r^q$ with constant emissivity index q, but even in the simple lamppost geometry there are significant departures at small radii, where the information about the spacetime geometry come from [83]. Meanwhile, at large scales there can be a variety of more subtle astrophysical

complications, including the possibility of disk warps or hotspots. Multiple ionization states, and a more detailed spectral modeling going beyond the iron line to consider the full reflection spectrum would also be important to consider (e.g., [82]). The impact of all these effects should be assessed. Here, our goal is to provide a first exploratory step along this path, in order to illuminate the most prominent effects and pave the way for followup studies.

6 Summary and conclusions

Astrophysical BH candidates are supposed to be the Kerr BHs predicted in general relativity, but the actual nature of these objects has still to be confirmed. The study of the properties of the electromagnetic radiation emitted by the gas in the accretion disk can be used to probe the spacetime geometry around these compact objects and hopefully test the Kerr BH hypothesis. Today, the continuum-fitting method and the analysis of the iron Kα line are the primary techniques capable of providing information about the metric around BH candidates. However, it is usually difficult to simultaneously constrain possible deviations from the Kerr solution, because there is a strong correlation between the measurement of the spin and the deformation parameters. In the end, non-Kerr BHs may look like Kerr BHs with a different spin parameter and, without an independent estimate of its spin, it is impossible to test their Kerr nature.

The iron Kα line is produced from the illumination of a cold disk by a hot corona above the accretion disk. Flaring regions in the corona produce fast time variability in the fluorescent line emission in the disk, manifesting in line reverberation. Because of insufficient count rates in present X-ray facilities in the iron-line band, to achieve sufficient signal one usually integrates for thousands of seconds. This causes a loss of information. Future X-ray facilities with larger effective areas may be capable of measuring the 2D transfer function; that is, the iron line signal as a function of time in response to an instantaneous coronal flare. The determination of the 2D transfer function can provide information about the spacetime geometry around the BH candidate, the geometry of the primary X-ray source, and the geometry of the accretion disk.

In this Paper, we report an exploratory and preliminary study on the impact of deviations from Kerr geometry on iron-line reverberation. We accordingly make simplistic and approximate predictions at the prospect of using iron-line reverberation to test the Kerr nature of BH candidates. In Section 4, we have considered a few specific examples for which we compare iron line profiles and 2D transfer functions in Kerr versus non-Kerr backgrounds. With the caution that we have adopted a simplified theoretical framework and not attempted to fully explore the correlations between all model parameters, our results indicate that reverberation measurements can provide stronger constraints on the spacetime geometry around astrophysical BH candidates with respect to time-integrated data. However, the difference is only substantial for high-signal data. With available X-ray facilities, even a good observation with $\sim 10^3$ photons in the iron line cannot distinguish a Kerr BH from a very deformed object. As an optimistic future observation, we have considered the case $N \sim 10^5$ and found that a similar observation can test the Kerr metric. From a simple interpolation between the case $N \sim 10^3$ and $N \sim 10^5$, we may expect that $\sim 10^4$ photons could already provide interesting constraints. Such results will hopefully be achieved in the near future with a generational improvement in X-ray instruments.

Although reverberation studies are already being used to glean information about relativistic effects in the inner reaches of AGN systems (see e.g Refs. [91–94]), for the precision

measurements we consider, the present fleet of X-ray detectors are unable to adequately resolve the transfer function at the required time plus energy resolution (they fall short of the mark for both stellar-mass and supermassive BH candidates). While a more detailed analysis beyond the scope of this work is necessary to properly assess the observability of non-Kerr deviations in reverberation data, our exploratory results indicate that a next-generation successor to *RXTE* [95] (such as *LOFT* [96] and possibly Athena [97]) might be capable of producing such measurements for a select few of the brightest and nearest AGN systems.

For instance, for *LOFT* observations of a nearby AGN, $z < 0.1$ with mass $\sim 10^9 M_\odot$, one may achieve *thousands* of photon counts in its reflection features, per unit M in time (i.e., bins of $\sim$ 5000s). The most prominent of these reflection features is that which we have emphasized throughout, namely the iron Kα line. Of course, in practice one may take advantage of signal from the *full* reflection spectrum, beyond just the iron line. Even while this domain becomes accessible to us for supermassive BH candidate systems, the timescales are sufficiently short for stellar-mass systems (i.e, tens of μs), that no detector now or on the immediate horizon, is likely to allow measurement of a transfer function in the relativistic regime for stellar-mass BH candidates.

Acknowledgments

We would like to thank Gary Hinshaw for useful comments and suggestions. JJ and CB were supported by the NSFC grant No. 11305038, the Shanghai Municipal Education Commission grant for Innovative Programs No. 14ZZ001, the Thousand Young Talents Program, and Fudan University. JFS was supported by the NASA Hubble Fellowship grant HST-HF-51315.01.

References

[1] B. Carter, Phys. Rev. Lett. **26**, 331 (1971).

[2] D. C. Robinson, Phys. Rev. Lett. **34**, 905 (1975).

[3] P. T. Chrusciel, J. L. Costa and M. Heusler, Living Rev. Rel. **15**, 7 (2012) [arXiv:1205.6112 [gr-qc]].

[4] R. Narayan, New J. Phys. **7**, 199 (2005) [gr-qc/0506078].

[5] R. H. Price, Phys. Rev. D **5**, 2419 (1972).

[6] R. H. Price, Phys. Rev. D **5**, 2439 (1972).

[7] C. Bambi, A. D. Dolgov and A. A. Petrov, JCAP **0909**, 013 (2009) [arXiv:0806.3440 [astro-ph]].

[8] C. Bambi, D. Malafarina and N. Tsukamoto, Phys. Rev. D **89**, 127302 (2014) [arXiv:1406.2181 [gr-qc]].

[9] F. Özel, D. Psaltis, R. Narayan and J. E. McClintock, Astrophys. J. **725**, 1918 (2010) [arXiv:1006.2834 [astro-ph.GA]].

[10] F. Özel, G. Baym and T. Guver, Phys. Rev. D **82**, 101301 (2010) [arXiv:1002.3153 [astro-ph.HE]].

[11] C. E. Rhoades and R. Ruffini, Phys. Rev. Lett. **32**, 324 (1974).

[12] V. Kalogera and G. Baym, Astrophys. J. **470**, L61 (1996).

[13] E. Maoz, Astrophys. J. **494**, L181 (1998) [astro-ph/9710309].

[14] R. Narayan and J. E. McClintock, New Astron. Rev. **51**, 733 (2008) [arXiv:0803.0322 [astro-ph]].

[15] A. E. Broderick, A. Loeb and R. Narayan, Astrophys. J. **701**, 1357 (2009) [arXiv:0903.1105 [astro-ph.HE]].

[16] C. M. Will, Living Rev. Rel. **9**, 3 (2006) [gr-qc/0510072].

[17] G. Dvali and C. Gomez, Fortsch. Phys. **61**, 742 (2013) [arXiv:1112.3359 [hep-th]].

[18] G. Dvali and C. Gomez, Phys. Lett. B **719**, 419 (2013) [arXiv:1203.6575 [hep-th]].

[19] S. B. Giddings, Phys. Rev. D **90**, no. 12, 124033 (2014) [arXiv:1406.7001 [hep-th]].

[20] F. D. Ryan, Phys. Rev. D **52**, 5707 (1995).

[21] K. Glampedakis and S. Babak, Class. Quant. Grav. **23**, 4167 (2006) [arXiv:gr-qc/0510057].

[22] L. Barack and C. Cutler, Phys. Rev. D **75**, 042003 (2007) [arXiv:gr-qc/0612029].

[23] T. A. Apostolatos, G. Lukes-Gerakopoulos and G. Contopoulos, Phys. Rev. Lett. **103**, 111101 (2009) [arXiv:0906.0093 [gr-qc]].

[24] D. F. Torres, Nucl. Phys. B **626**, 377 (2002) [hep-ph/0201154].

[25] C. Bambi and E. Barausse, Astrophys. J. **731**, 121 (2011) [arXiv:1012.2007 [gr-qc]].

[26] C. Bambi, Astrophys. J. **761**, 174 (2012) [arXiv:1210.5679 [gr-qc]].

[27] L. Kong, Z. Li and C. Bambi, Astrophys. J. **797**, 78 (2014) [arXiv:1405.1508 [gr-qc]].

[28] Y. Lu and D. F. Torres, Int. J. Mod. Phys. D **12**, 63 (2003) [astro-ph/0205418].

[29] T. Johannsen and D. Psaltis, Astrophys. J. **773**, 57 (2013) [arXiv:1202.6069 [astro-ph.HE]].

[30] C. Bambi, Phys. Rev. D **87**, 023007 (2013) [arXiv:1211.2513 [gr-qc]].

[31] T. Johannsen and D. Psaltis, Astrophys. J. **726**, 11 (2011) [arXiv:1010.1000 [astro-ph.HE]].

[32] C. Bambi, JCAP **1209**, 014 (2012) [arXiv:1205.6348 [gr-qc]].

[33] A. N. Aliev, G. D. Esmer and P. Talazan, Class. Quant. Grav. **30**, 045010 (2013) [arXiv:1205.2838 [gr-qc]].

[34] C. Bambi, JCAP **1308**, 055 (2013) [arXiv:1305.5409 [gr-qc]].

[35] C. Bambi and K. Freese, Phys. Rev. D **79**, 043002 (2009) [arXiv:0812.1328 [astro-ph]].

[36] C. Bambi and N. Yoshida, Class. Quant. Grav. **27**, 205006 (2010) [arXiv:1004.3149 [gr-qc]].

[37] C. Bambi, Phys. Rev. D **87**, 107501 (2013) [arXiv:1304.5691 [gr-qc]].

[38] Z. Li and C. Bambi, JCAP **1401**, 041 (2014) [arXiv:1309.1606 [gr-qc]].

[39] K. Liu, N. Wex, M. Kramer, J. M. Cordes and T. J. W. Lazio, Astrophys. J. **747**, 1 (2012) [arXiv:1112.2151 [astro-ph.HE]].

[40] Z. Li and C. Bambi, Phys. Rev. D **90**, 024071 (2014) [arXiv:1405.1883 [gr-qc]].

[41] F. Atamurotov, A. Abdujabbarov and B. Ahmedov, Phys. Rev. D **88**, 064004 (2013).

[42] C. Bambi, Mod. Phys. Lett. A **26**, 2453 (2011) [arXiv:1109.4256 [gr-qc]].

[43] C. Bambi, Astron. Rev. **8**, 4 (2013) [arXiv:1301.0361 [gr-qc]].

[44] S. N. Zhang, W. Cui and W. Chen, Astrophys. J. **482**, L155 (1997) [astro-ph/9704072].

[45] L. -X. Li, E. R. Zimmerman, R. Narayan and J. E. McClintock, Astrophys. J. Suppl. **157**, 335 (2005) [astro-ph/0411583].

[46] J. E. McClintock, R. Narayan, S. W. Davis, L. Gou, A. Kulkarni, J. A. Orosz, R. F. Penna and R. A. Remillard *et al.*, Class. Quant. Grav. **28**, 114009 (2011) [arXiv:1101.0811 [astro-ph.HE]].

[47] J. E. McClintock, R. Narayan and J. F. Steiner, Space Science Reviews 73 (2014) [arXiv:1303.1583 [astro-ph.HE]].

[48] A. C. Fabian, M. J. Rees, L. Stella and N. E. White, Mon. Not. Roy. Astron. Soc. **238**, 729 (1989).

[49] A. C. Fabian, K. Iwasawa, C. S. Reynolds and A. J. Young, Publ. Astron. Soc. Pac. **112**, 1145 (2000) [astro-ph/0004366].

[50] L. Brenneman, *Measuring the Angular Momentum of Supermassive Black Holes*, (SpringerBriefs in Astronomy, ISBN 978-1-4614-7770-9, 2013).

[51] C. S. Reynolds, Space Science Reviews 81 [arXiv:1302.3260 [astro-ph.HE]].

[52] J. F. Steiner, J. E. McClintock, R. A. Remillard, L. Gou, S. 'y. Yamada and R. Narayan, Astrophys. J. **718**, L117 (2010) [arXiv:1006.5729 [astro-ph.HE]].

[53] J. E. McClintock, R. Shafee, R. Narayan, R. A. Remillard, S. W. Davis and L. X. Li, Astrophys. J. **652**, 518 (2006) [astro-ph/0606076].

[54] A. Sadowski, M. Abramowicz, M. Bursa, W. Kluzniak, J. P. Lasota and A. Rozanska, Astron. Astrophys. **527**, A17 (2011) [arXiv:1006.4309 [astro-ph.HE]].

[55] S. E. Motta, T. M. Belloni, L. Stella, T. Muoz-Darias and R. Fender, Mon. Not. Roy. Astron. Soc. **437**, 2554 (2014) [arXiv:1309.3652 [astro-ph.HE]].

[56] S. E. Motta, T. Muoz-Darias, A. Sanna, R. Fender, T. Belloni and L. Stella, Mon. Not. Roy. Astron. Soc. **439**, 65 (2014) [arXiv:1312.3114 [astro-ph.HE]].

[57] G. Risaliti, E. Nardini, M. Elvis, L. Brenneman and M. Salvati, Mon. Not. Roy. Astron. Soc. **417**, 178 (2011) [arXiv:1105.2318 [astro-ph.CO]].

[58] M. Middleton and A. Ingram, Mon. Not. Roy. Astron. Soc. **446**, 1312 (2015) [arXiv:1410.5992 [astro-ph.HE]].

[59] C. Bambi, arXiv:1312.2228 [gr-qc].

[60] C. Bambi, Phys. Rev. D **85**, 043002 (2012) [arXiv:1201.1638 [gr-qc]].

[61] C. Bambi, Phys. Rev. D **86**, 123013 (2012) [arXiv:1204.6395 [gr-qc]].

[62] Z. Li, L. Kong and C. Bambi, Astrophys. J. **787**, 152 (2014) [arXiv:1401.1282 [gr-qc]].

[63] N. Tsukamoto, Z. Li and C. Bambi, JCAP **1406**, 043 (2014) [arXiv:1403.0371 [gr-qc]].

[64] C. Bambi and D. Malafarina, Phys. Rev. D **88**, 064022 (2013) [arXiv:1307.2106 [gr-qc]].

[65] C. Bambi, Phys. Rev. D **87**, 084039 (2013) [arXiv:1303.0624 [gr-qc]].

[66] C. Bambi, Phys. Lett. B **730**, 59 (2014) [arXiv:1401.4640 [gr-qc]].

[67] C. Bambi, Phys. Rev. D **90**, 047503 (2014) [arXiv:1408.0690 [gr-qc]].

[68] D. R. Wilkins and L. C. Gallo, Mon. Not. Roy. Astron. Soc. **448**, 703 (2015) [arXiv:1412.0015 [astro-ph.HE]].

[69] P. Uttley, I. M. McHardy and S. Vaughan, Mon. Not. Roy. Astron. Soc. **359**, 345 (2005) [astro-ph/0502112].

[70] L. Stella, Nature **344**, 747 (1990).

[71] G. Matt and C. Perola, Mon. Not. Roy. Astron. Soc. **259**, 433 (1992).

[72] C. S. Reynolds, A. J. Young, M. C. Begelman and A. C. Fabian, Astrophys. J. **514**, 164 (1999) [astro-ph/9806327].

[73] G. Matt, G. C. Perola and L. Piro, Astron. Astrophys. **247**, 25 (1991).

[74] A. Martocchia and G. Matt, Mon. Not. Roy. Astron. Soc. **282**, L53 (1996).

[75] B. Czerny and A. Janiuk, Astron. Astrophys. **464**, 167 (2007) [astro-ph/0612262].

[76] J. D. Schnittman and J. H. Krolik, Astrophys. J. **712**, 908 (2010) [arXiv:0912.0907 [astro-ph.HE]].

[77] C. Done, S. Davis, C. Jin, O. Blaes and M. Ward, Mon. Not. Roy. Astron. Soc. **420**, 1848 (2012) [arXiv:1107.5429 [astro-ph.HE]].

[78] I. D. Novikov, K. S. Thorne, "Astrophysics of Black Holes" in *Black Holes*, edited by C. De Witt and B. De Witt (Gordon and Breach, New York, New York, 1973), pp. 343-450.

[79] D. N. Page and K. S. Thorne, Astrophys. J. **191**, 499 (1974).

[80] I. M. George, A. C. Fabian, Mon. Not. Roy. Astron. Soc. **249**, 352 (1991).

[81] R. R. Ross, A. C. Fabian, Mon. Not. Roy. Astron. Soc. **358**, 211 (2005) [arXiv: 0501116 [astro-ph]].

[82] J. Garcia, T. Dauser, A. Lohfink, T. R. Kallman, J. F. Steiner, J. E. McClintock, L. Brenneman and J. Wilms *et al.*, Astrophys. J. **782**, 76 (2014) [arXiv:1312.3231 [astro-ph.HE]].

[83] T. Dauser, J. Garcia, J. Wilms, M. Bock, L. W. Brenneman, M. Falanga, K. Fukumura and C. S. Reynolds, Mon. Not. Roy. Astron. Soc. **430**, 1694 (2013) [arXiv:1301.4922 [astro-ph.HE]].

[84] A. R. King, S. H. Lubow, G. I. Ogilvie, and J. E. Pringle, Mon. Not. Roy. Astron. Soc. **363**, 49 (2005) [arXiv: 0507098 [astro-ph]].

[85] Y. Zhu, S. W. Davis, R. Narayan, A. K. Kulkarni, R. F. Penna and J. E. McClintock, Mon. Not. Roy. Astron. Soc. **424**, 2504 (2012) [arXiv:1202.1530 [astro-ph.HE]].

[86] J. D. Schnittman, J. H. Krolik and S. C. Noble, Astrophys. J. **769**, 156 (2013) [arXiv:1207.2693 [astro-ph.HE]].

[87] T. Johannsen and D. Psaltis, Phys. Rev. D **83**, 124015 (2011) [arXiv:1105.3191 [gr-qc]].

[88] B. M. Peterson, *An introduction to active galactic nuclei* (Cambridge University Press, Cambridge, UK, 1997).

[89] E. M. Cackett, A. Zoghbi, C. Reynolds, A. C. Fabian, E. Kara, P. Uttley and D. R. Wilkins, Mon. Not. Roy. Astron. Soc. **438**, 2980 (2014) [arXiv:1311.2997 [astro-ph.HE]].

[90] D. R. Wilkins and A. C. Fabian, Mon. Not. Roy. Astron. Soc. **424**, 1284 (2012) [arXiv:1205.3179 [astro-ph.HE]].

[91] A. Zoghbi, A. Fabian, P. Uttley, G. Miniutti, L. Gallo, C. Reynolds, J. Miller and G. Ponti, Mon. Not. Roy. Astron. Soc. **401**, 2419 (2010) [arXiv:0910.0367 [astro-ph.HE]].

[92] A. Zoghbi, A. C. Fabian, C. S. Reynolds and E. M. Cackett, Mon. Not. Roy. Astron. Soc. **422**, 129 (2012) [arXiv:1112.1717 [astro-ph.HE]].

[93] E. Kara, A. C. Fabian, E. M. Cackett, J. F. Steiner, P. Uttley, D. R. Wilkins and A. Zoghbi, Mon. Not. Roy. Astron. Soc. **428**, 2795 (2013) [arXiv:1210.1465 [astro-ph.HE]].

[94] D. Emmanoulopoulos, I. E. Papadakis, M. Dovciak and I. M. McHardy, Mon. Not. Roy. Astron. Soc. **439**, 3931 (2014) [arXiv:1402.0899 [astro-ph.HE]].

[95] J. H. Swank, Nucl. Phys. B Proc. Suppl. **69**, 12 (1999) [astro-ph/9802188].

[96] M. Feroci, L. Stella and M. van der Klis *et al.*, Experimental Astronomy **34**, 415 (2012).

[97] K. Nandra, D. Barret, X. Barcons, A. Fabian, J. W. d. Herder, L. Piro, M. Watson and C. Adami *et al.*, arXiv:1306.2307 [astro-ph.HE].